Erosion evolution in mono-crystalline silicon surfaces caused by acoustic cavitation bubbles

David Fernandez Rivas, Joris Betjes, Bram Verhaagen, Wilco Bouwhuis, Ton C. Bor et al.

Additional information on J. Appl. Phys.

Erosion evolution in mono-crystalline silicon surfaces caused by acoustic cavitation bubbles

David Fernandez Rivas,[1,a)] Joris Betjes,[1] Bram Verhaagen,[2] Wilco Bouwhuis,[3] Ton C. Bor,[4] Detlef Lohse,[3] and Han J. G. E. Gardeniers[1]

[1]*Mesoscale Chemical Systems Group, MESA + Research Institute, University of Twente, ME147, P.O. Box 217, 7500 AE Enschede, The Netherlands*
[2]*Physics of Fluids Group and MIRA Research Institute, Faculty of Science and Technology, University of Twente, P.O. Box 217, 7500 AE Enschede, The Netherlands*
[3]*Physics of Fluids Group and MESA + Research Institute, Faculty of Science and Technology, University of Twente, P.O. Box 217, 7500 AE Enschede, The Netherlands*
[4]*Chair of Production Technology, Faculty of Engineering Technology, University of Twente, P.O. Box 217, 7500 AE Enschede, The Netherlands*

The early stages (<180 min) of cavitation erosion of silicon surfaces were studied for three different crystallographic orientations. We introduce a quantity defined as the ratio of the relative eroded area to the number of pits, α_p, to evaluate the evolution of erosion among the different substrates used. Different erosion evolution was observed for (100), (110), and (111) silicon surfaces when exposed to cavitation bubbles generated by an ultrasound signal of 191 kHz. (100) silicon substrates showed the most erosion damage, with an eroded area 2.5 times higher than the other two crystallographic orientation substrates after 180 min sonication. An apparent incubation period of 50 min was measured. The number of erosion pits increased monotonically for (110) and (111), but for (100) no increase was detected after 120 min. The collapse of a spherical bubble was simulated using an axisymmetry boundary integral method. The calculated velocity of the jet from the collapsing bubble was used to estimate the pressure P that is induced by the jet upon impact on the silicon substrate. © 2013 American Institute of Physics. [http://dx.doi.org/10.1063/1.4791582]

INTRODUCTION

From cavitation bubbles to erosion

In 1894 Sir. John I. Thornycroft and Sydney W. Barnaby found bubble formation (cavities) on spinning propeller and speculated that it was connected to vibration and erosion of the propeller. Later on, the English Royal Navy approached John William Strutt (Lord Rayleigh) to study the causes for the damage found on boat and submarine propellors moving at high speeds.[1–3] Rayleigh confirmed that this damage was due to cavitation bubbles. Cavitation is defined as the growth and collapse of a gaseous void when an external negative pressure is applied to a liquid volume.[4,5] The ship propellers rotate fast enough to reduce the pressure in the liquid near the blades below the water vapor pressure, leading to the formation of bubbles. The subsequent bubble collapse can be so violent that materials as hard as steel can be severely damaged, which is referred to as cavitation damage. In the past decades, cavitation damage has been of interest in engineering since it is an undesirable effect in, among others, artificial heart valves, hydraulic machinery, and bearings.[6–8] The mechanical effects of ultrasound cavitation have found several other applications in the last decade, such as cleaning of surfaces, the development and optimization of new coatings, surface functionalizations, nanofoams and several other used in solar cells, imaging sensors, mechanical parts, and hip prostheses.[9–18] As an example, it is possible to make Si surfaces porous by exposure to ultrasound cavitation which can be used as photoluminescent structure, additionally reducing aging effects of the Si surface.[14,19–21]

Cavitation is influenced by several parameters such as saturating gas, pressure amplitude, and temperature, which are interconnected and are hard to fine-tune.[22] In practical situations, bubbles frequently nucleate from defects on the wall of the container or on dissolved particles, where small pockets of gas are trapped (heterogeneous cavitation). Controlled formation of cavitation bubbles can be achieved by using for example a laser, shockwaves, or ultrasound equipment.[23–28] Here, we use an ultrasound device employing micropits that has been shown recently[10] to enable the control of the location and amount of cavitation and the surface modification effects on a millimeter scale.

Cavitation bubbles display a rich behavior. When bubbles undergo stable cavitation, acoustic streaming and shear forces on the surrounding medium are generated. Very high fluid velocities, pressure and temperatures, and shock wave emission can occur. The presence of a boundary or other bubbles breaks the symmetry around an otherwise spherical collapsing bubble, leading to a high-velocity jet. The velocity of such a jet can be of the order of 100 m/s.[29,30]

Secondary effects of inertial bubble collapse include bubble fragmentation, splashing, and deformation of the walls nearby the collapsing bubble.[4,11,24,30–34]

The majority of literature agrees that the destructive action of cavitation bubbles is due mainly to two phenomena: the generation of the high-speed liquid jet directed

a)Electronic mail: d.fernandezrivas@utwente.nl. Tel.: +31 53 489 2594.

towards the (solid) boundary and the emission of shock waves upon the collapse of the bubble.

Frequency is an important parameter that will determine several effects of cavitation such as the size of bubbles, surface modifications, chemical effects and light emission, to name a few.[13,22,35,36] At lower frequencies (ca. 20 kHz), physical surface modification occurs mainly due to the effect of energetic micro-jetting, modifying the surface morphology with high weight loss.[13]

For higher frequencies (up to 150 kHz), the pressure field, luminescence, and locations where erosion occurred, coincided with less erosion and was attributed to damped cluster collapse.[37] The concerted collective action of cavities is known to give rise to pressures at the target surface as high as 900 MPa.[38]

When a surface is impacted (jetting or shockwave), stress waves are generated and propagate in the solid, which can generate damage not only to the surface but also to the bulk.[18,39] Two basic types of stress waves exist in solids, namely body and surface waves. Compression waves propagate in the body; the shear and surface waves are of the Rayleigh type.

The orientation and velocity of a liquid jet and the severity of the collapse and subsequent effect will depend on the impedance of the material loaded and its stand-off distance γ from the boundary. Near a hard boundary, the jet will form towards the boundary, whereas near a soft boundary, the jet may form away from the wall and thereby pull on the wall.[30,40]

Ohl *et al.*[41] were able to locate the origin of two shock waves as the separate emission of a jet-induced and a bubble-collapse-induced shock wave. A shock wave is generated by the impact of the jet tip onto the lower bubble wall (jet shock wave).[30] The pressure acting on a rigid wall due to a shock wave can be of the order of 10 GPa.[34] During cloud rebound after the collapse of a hemispherical cloud of bubbles close to a rigid boundary, secondary shock wave emissions occur.

It has been shown that the spherical shock waves arising in a liquid during cavitation bubble collapse lead to the formation of deep needle-like pits on the solid surface.[38] This damage is caused by the spallation due to interference of rarefaction waves, and it was found for several materials such as steel and duraluminum. Spallation was defined as dynamic damage taking place upon focusing or interference of rarefaction waves. Several spall cracks in the material yield fragmentation and detachment of material grains, forming craters.

Cavitation erosion in silicon

The effects of microbubble cavitation close to silicon surfaces in a micro-sono-reactor have been described in previous publications.[27,28,42] Within 5 min of exposure to cavitation bubbles nucleated from pits, a region of damaged silicon substrate was observed near the region where bubbles collapsed. Remarkably, the shape of the individual damage sites coincided with the {111} crystal planes of the crystalline structure of the silicon (100) wafers used. In connection to surface damage, the emission of shock waves by collapsing

bubbles and jetting towards the silicon surfaces was highlighted as possible causes. The current study will attempt to obtain more details on erosion evolution in silicon substrates. Additionally, the setup may be used not only to test the erosion on the surface with the etched pits, but in a similar way as presented before,[10] on another surface in the vicinity of the bubble generation.

A pioneering work on this subject was published in 1965 by Howkins.[25] An air bubble was trapped in a hole (1 mm diameter and depth) drilled into a surface, immersed in water, and vibrated. When exposed to ultrasound at 20 kHz with degassed water and water saturated with air, the erosion in a nearby brass surface was studied, giving erosion even at ultrasound amplitudes at which, in the absence of the trapped bubble, no erosion took place.

More recently,[18] the physicochemical behavior of crystalline silicon (100) under acoustic cavitation was investigated in water sparged with argon. Ar* emissions generated by mechanoluminescence (emission of light caused by mechanical action on a solid[43]) were detected. Besides physical and chemical changes in the Si surface that altered wetting properties and topology, phase transformations of the Si lattice were studied with Raman spectroscopy and transmission electron microscopy (TEM). Long incubation periods of erosion were found with cracks and defect cleavages aligned with the crystallographic lattice in agreement with the brittle nature of Si at room temperature. Interestingly, local disorder damage was found in line with plastic deformations.[18]

Here, we investigate erosion of silicon surfaces. Silicon has a diamond face-centred cubic crystal structure (fcc). Slip in silicon occurs on {111} slip planes with Burgers vectors of a/2 $\langle 1\bar{1}0 \rangle$ and a/6 $\langle 11\bar{2} \rangle$ types.[44] The angles (ϕ) between planes of the family {100} and {110} are 45° or 90°. Between {100} and {111} planes, the intersection angle is 54.7°. Furthermore, {111} and {110} planes intersect under 35.3°, 90°, or 144.7°.[45] Figure 1 illustrates these orientations schematically.

Erosion evolution

Studies of cavitation erosion have covered a wide variety of materials and conditions, from ductile metals, brittle plastics, ceramics, and soluble materials to glass.[11,39,46–48] All materials have intrinsic defects in its surface and bulk. When exposed to cavitation activity, regularly an incubation period occurs where small deformations (erosion pits) appear on the surface after short duration exposure, or the existing defects start to grow. These defects can serve as heterogeneous nucleation sites and promote cavitation erosion. As exposure to cavitation continues, different behaviors are observed depending on the nature of the material. The erosion can accelerate and eventually reach a stable erosion rate.[31,49,50]

When cyclic stresses of a given load are applied for a certain time, most materials degrade and can suffer premature failure. This phenomenon is known as fatigue and is the most commonly experienced form of structural failure, yet it is one of the least understood for single crystalline silicon.[51]

Brittle materials, such as single crystal silicon at room temperature, have very limited dislocation mobility, making
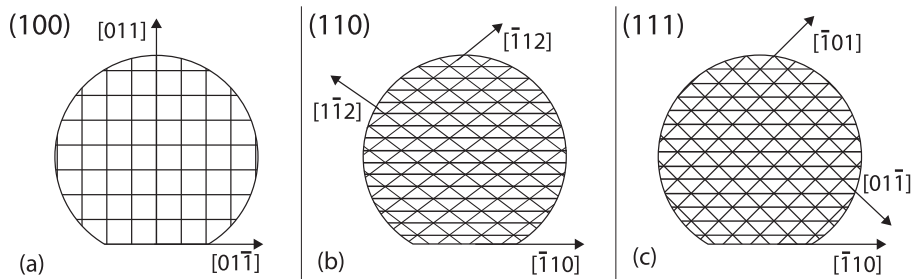
FIG. 1. Sketch of the crystallographic plane configuration in mono-crystalline silicon for (a) (100), (b) (110), and (c) (111). All lines are the intersecting {111} planes with each corresponding specific top surface plane.

the possibility of cyclic fatigue failure not obvious. The durability and reliability assessment of microscale devices (air bags, blood pressure sensors, and jet cartridge nozzles) has driven studies on the fatigue effect on materials used in the semiconductor industry.[52] The fatigue damage accumulation in silicon can take place with the detachment of inclined {111} planes on the fracture surface when energy is dissipated, forming cleavage planes.[51,52]

The cracking behavior of Si is not that well reported in the literature. The corresponding mechanisms of fatigue in brittle materials, such as the structural films commonly used in MEMS, are quite different from the generation and motion of dislocations and the accumulation of plastic deformation in metals. The {111} and {110} planes are known to be preferred cleavage planes, which means that cracks propagate preferentially along them. Reported values of the fracture toughness are given in Table I, but do not differ much from each other.

The influence of the environmental conditions on Si fatigue in air and water has also been tested with the conclusion that the fracture surface in water consists of several fracture planes (failed by several cracks), whereas the one in air is a single plane (single crack).[53] Apparently, water influences the oxidation of the silicon surface and accelerates the erosion-fatigue effects. A similar effect occurs for glass surfaces where silanol forms.[54]

Ultrasound cavitation can have an etching effect induced by the formation of monohydrides to the detriment of multihydride formation. Ultrasound cavitation can also lead to porous layers with decreased oxidation and hydrogenation.[20]

Quantifying cavitation erosion

Materials erosion is a complex phenomenon in itself, and due to the rich behavior of bubbles, we find an even more complex correlation in cavitation erosion. Methods for quantifying erosion strongly depend on the device, ultrasound frequency, material, and its orientation and prepara-

tion, and exposure time. A popular method to quantify or map cavitational erosion effects has been to damage aluminum foils.[30,31] However, the results cannot be extrapolated to other materials. The relation between impact load by collapsing cavitation bubbles and erosion damage can be addressed by measuring impact loads and erosion damage with sophisticated equipment.[55]

Several single-number parameters like the volume loss, the mass loss, and the mean and maximum depth of erosion penetration are determined after exposure to cavitation in order to quantify the amount of erosion that has taken place. Additionally, the instantaneous erosion rate, the mean depth of erosion penetration rate, the incubation period, and the time needed to achieve the maximum damage rate are used to characterize a given period of erosion progress.

Efforts to standardize existing erosion test methods have had limited success.[56] As the damage rates of different materials depend on so many factors, the realistic loading of the material under field conditions is usually unknown. Often ultrasonic horns or baths are used; obviously each of them has limitations in the range of frequencies, operational power, and pressure values. Also, as erosion at early stages is so small, it is not possible to measure erosion by weighing the samples before and after ultrasound exposure.

In this paper, we demonstrate that an ultrasound device with a silicon substrate with micropits can be used effectively to study the erosion of silicon. Other materials may be used as well with this approach. Using high-resolution scanning electron microscopy (SEM) imaging, information on the evolution and extend of cavitation erosion can be obtained in a quantitative way, allowing for comparison of the erosion of different materials.

Varvani-Farahani[57] proposed a model to obtain the number of cycles for fatigue failure of silicon to occur, in which the total fatigue damage is accumulated as the number of cycles progresses. Here, we attempt to relate the number of cycles to erosion by measuring the amount of erosion after a certain cavitation exposure time and correlating that to the calculated expected number of cavitation bubbles.

TABLE I. Physical properties of mono-crystalline silicon crystal planes.

Crystal planes	{100}	{110}	{111}
Surface energy[a] (J/m^2)	1.99	1.41	1.15
Modulus of elasticity[b] ($\times 10^{11}$ Pa)	1.40	2.13	2.46
Fracture toughness[c] (MPa m$^{1/2}$)	0.95	0.90	0.82

[a]Reference 70.
[b]Reference 71.
[c]Reference 72.

EXPERIMENTAL SECTION

Ultrasound setup

Experiments were conducted with 1×1 cm^2 square micromachined chips silicon single crystalline with orientation $\langle 100 \rangle$, $\langle 110 \rangle$, and $\langle 111 \rangle$ (Okmetic, Vantaa, Finland). The chips were diced from different p-type polished wafers with a smooth surface (3.46–4.22 Å). Two pits were

micromachined in the surface with an inter-pit distance of $100 \, \mu m$; each pit has a diameter of $30 \, \mu m$ and a depth of $\sim 10 \, \mu m$. Further details on the fabrication of the micromachined pits on the substrates can be found elsewhere.[27,28,42]

The glass cavitation cell, in which the substrates were placed, was glued to a piezo element and details can be found elsewhere.[27,28,42] An Agilent 33250 A 80 MHz wave generator provided a 191 KHz sinusoidal signal, which was amplified by a Sony TA-FB 740FBR amplifier to 0.07 ± 0.01 W, providing an acoustic density of 0.14 W/cm^2. The bottom of the piezo element was in contact with a Marlow Industrial Peltier-element to keep the temperature at $23 \pm 1 \, ^\circ$C. A heat sink and fan were placed underneath the piezo element to remove excess heat. A glass slide and rubber ring were placed over the reaction cell to reduce evaporation of the liquid during the experiments. A Multimetrix DMM220 multimeter connected to a 0.2 mm diameter T-type thermocouple was used to measure the temperature within the reaction cell. The current and voltage supplied to the piezo element were monitored with a HAMEG HM 8115-2 power meter.

High-speed visualization setup for bubble dynamics

The generation of cavitation from the micropits was visualized using two cameras. One was the ultra-high speed camera facility (Brandaris 128),[58] which recorded 6 movies (spaced 20 ms apart) of 128 frames at a frame rate of approximately 10 Mfps. The other was the Photron, model SA1.1 with framerates up to 500 kfps. A microscope (BX-FM, Olympus) provided $20\times$ magnification; illumination was provided in dark-field mode using a Xenon flash source.

A second system reported before,[28,59] which is able to capture single snapshots with a short exposure time, was used to image shockwave emissions. The camera was a Lumenera LM165 with a sensitive Sony EXview HAD CCD sensor. The Olympus microscope was equipped with two long working distance (WD) objectives, the *LMPLFLN* $10\times$ (WD 21 mm/NA = 0.25) and the *SMPLFLN* $20\times$ (WD 25 mm/NA = 0.25) both Olympus. A bright laser-induced fluorescence pulse of 7 ns duration (full width at half maximum) was used for illumination, amounting to about one thousandth of the acoustic period, providing high-resolution images without motion blur.

Numerical modeling of single bubble collapse near a solid wall

The collapse of a spherical bubble was simulated using an axisymmetric boundary integral (BI) method, see Appendix for details and Figure 3 for a schematic representation. The BI simulation tracked the interface of the bubble up to the point where the two opposite interfaces of the axisymmetric bubble touched each other. The velocity difference of these two interfaces at this instant was used as an approximation of the velocity V of the jet from the collapsing bubble.

The pressure P that is induced by the jet upon impact on the silicon substrate can be estimated calculating the water hammer pressure[60]

$$P = \frac{\rho_1 C_1 \rho_2 C_2 V}{\rho_1 C_1 + \rho_2 C_2} \qquad (1)$$

with ρ the density and C the speed of sound in the liquid (subscript 1) and the silicon (subscript 2). The water hammer pressure is associated with the shock wave induced by the impact of a liquid cylinder onto a solid surface.[61]

The wall shear stress is estimated from the Glauert solution for the wall jet, as outlined by Ohl *et al.*,[62] and evaluated at a distance of one jet diameter away from the center of the jet. The jet diameter is estimated to be a fraction of the maximum radius of the bubble $R_{max}/60$.[63]

Silicon surfaces selection and cavitation exposure

Table I summarizes the most important mechanical properties of {100}, {110}, and {111} cleavage planes of silicon. The differences reported by different authors are mainly due to the ways the measurements are carried out and by the exact lattice orientation which can vary from one manufacturer to another.[64–69]

All substrates were cleaned using a VWR ultrasonic cleaner at 20 kHz for 5 min, Olympus lens cleaner tissues, and three chemicals (acetone, alcohol, and milliQ water). The beaker was moved constantly in order to avoid stable bubbles collapsing against the silicon substrate. The cleaned substrates were dried with inert nitrogen and placed into the glass reaction cell. Using an Eppendorf $300 \, \mu L$ pipette, milliQ water was poured in the reaction cell containing the substrate. The water temperature inside the reaction chamber was measured and a rubber ring and glass slide were placed on the reaction chamber. The Peltier-element was set at 0.80 V to keep the temperature constant at $23 \, ^\circ$C.

The substrates were exposed to US for different time intervals ranging from 5 to 60 min in different rounds. The final exposure time achieved was 180 min. At the end of each experiment, the substrate was removed and the reaction cell was dried with nitrogen. This procedure was repeated for every measurement.

An oxygen plasma cleaner barrel Tepla 300E was used to remove carbonaceous contamination.

Fractography, imaging, and processing

The silicon substrate surfaces were imaged using SEM before and after erosion took place, also termed fractography. The surface topology of each surface provides information on the damage initiation sites and the possible failure mechanisms. The fractography in our study was done with a High Resolution SEM Zeiss 1550 under a vacuum of 5×10^{-7} Pa. The substrates were imaged within the region of the two micromachined pits where cavitation bubbles were present. The images were made perpendicular to the specimen surface with electron energies of 5 keV and 100 keV with a resolution of 1023×767 pixels. We did not follow the growth of individual erosion pits in time, since each SEM analysis was performed at a magnification large enough to provide good resolution, but no complete coverage was possible. The scans were always done in the same region, but after the plasma cleaning step needed to remove
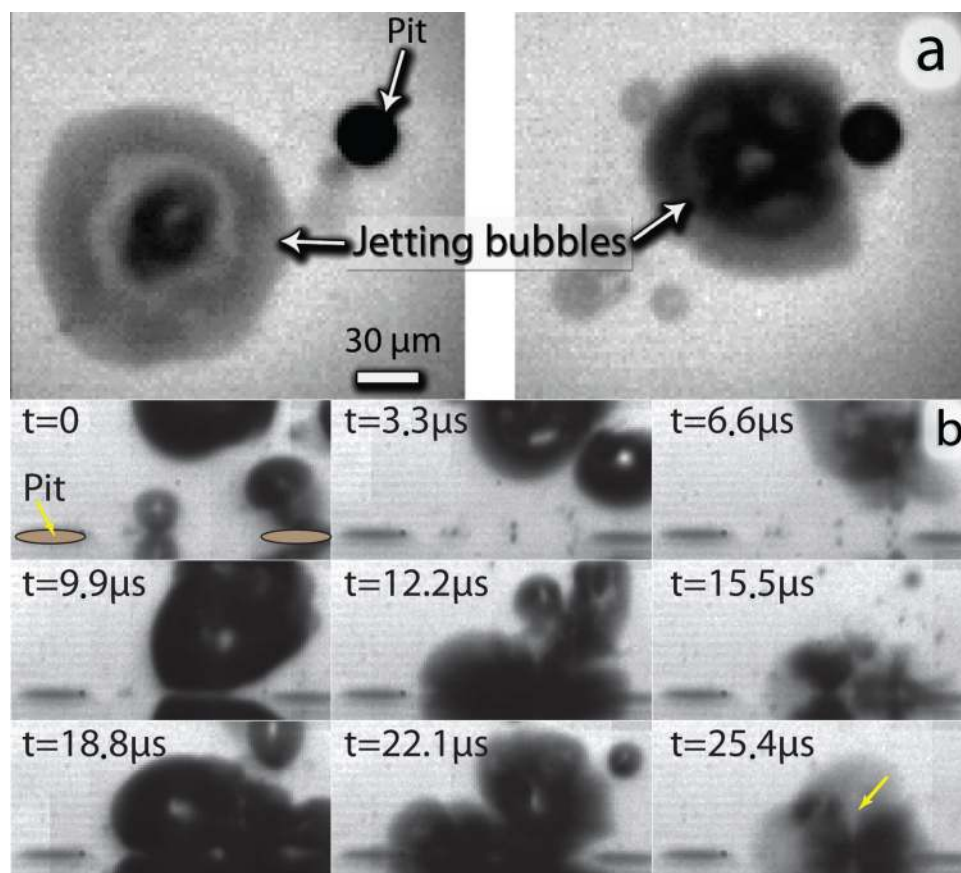
FIG. 2. (a) Top view of bubbles cavitation close to the silicon surface. The pit has a diameter of 30 μm. These are individual snapshots taken at 100 kfps and 0.1 μs exposure time. (b) Side view of bubbles cavitation close to the silicon surface after being ejected from two pits of 30 μm diameter at a distance of 100 μm. In t = 0, a bubble ejects from the pit to the right. Subsequent collapses, coalescence and jetting towards the surface (as well as among bubbles) can be seen in all frames, particularly the arrow at t = 25.4 μs. There are two images per each acoustic cycle.

carbonaceous contamination, it is virtually impossible to find exactly the same erosion pit.

Using the Image Processing Toolbox of MATLAB R2011A, an in-house developed script was used to post-process the SEM images. ImageJ processing software was used to perform filtering and noise reduction. For each SEM image, the erosion pit boundaries and areas were determined. The total eroded area ΔA was registered as well as the total area processed A.

The erosion pit depth was estimated for the (100) Si substrates using trigonometry; for an erosion pit having an isosceles triangle cross-section shape, the depth (d) was calculated with $d = \frac{w}{2} \times \tan(54.7°)$; w being the smallest side of the erosion pit used as the base width.

Sonication using an ultrasonic horn at 20 kHz

A Branson 250 Sonifier (Danbury CT, USA) of the horn type with a microtip of diameter 3 mm was used to compare the effects of cavitation bubbles generated with a conventional ultrasonic device. The frequency of such a device is 20 kHz and the power provided to the tip is limited by the hardware manufacturer to 70% of the nominal power of the power supply (200 W).

Polished p-type silicon chips with crystallographic orientation (100), (110), and (111) parallel to the surface were taped to the bottom of a beaker filled with 500 ml of water and placed on an adjustable stage. The ultrasonic horn was set with a ring stand, and the horn tip was placed perpendicular to the silicon substrate at 0.5 mm. The substrates were exposed

to cavitation for 5, 10, and 15 min. These irradiation times and conditions are supposed to fall within the incubation-acceleration period.[18]

RESULTS

Cavitation bubbles: Observations and simulation results

The nucleation of bubbles from stabilized bubbles on micromachined pits on silicon surfaces has been described in detail elsewhere.[27,28,42] In short, and observed in the ultra-high speed recordings, the bubble stabilized on the pit oscillates and sheds off micron sized bubbles with an average radius and number that depends on the power applied (pressure amplitude). The conditions of the experiment described here are similar to the case of one pit and high power setting described previously, and account for a most probable bubble radius of 2 μm, average equivalent bubble radius of 8 μm and 50 bubbles per acoustic cycle. Figure 2 shows a top-view example of cavitation around two pits.

The nucleation of bubbles can be sustained for several hours as long as the conditions are kept constant (avoiding liquid evaporation, constant temperature, etc.) by virtue of a phenomenon similar to rectified diffusion.[28] The nucleated bubbles are observed to break up seeding the liquid with their fragments, a cycle of expansion, collapse, break-up, and again expansion. Since the driving ultrasound amplitude was high enough to obtain large and deforming bubbles, they tended to collapse against the surface producing impinging liquid jets. See Figure 2 for a side view.
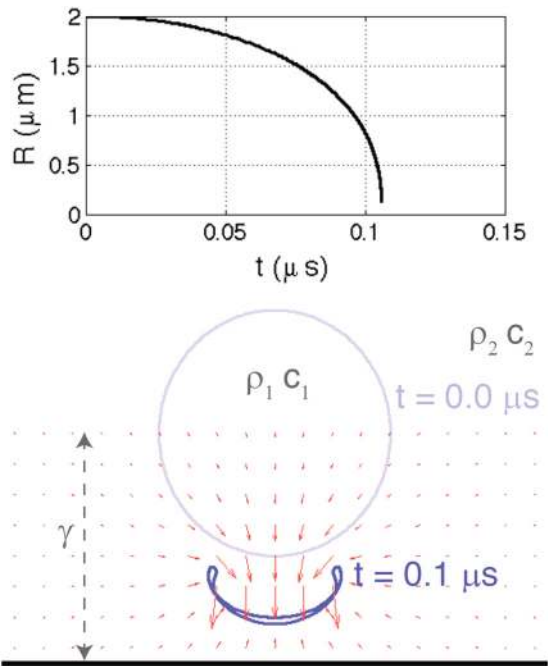
FIG. 3. Example of a radius-time curve (top) and vector field (bottom; blue is the bubble contour, red are the fluid velocity vectors) as calculated by the axisymmetric BI code for a $R = 2 \mu m$ initial radius bubble at $\gamma = 4 \mu m$ from the wall. ρ_1, C_1 stand for vapor density and sound speed, whereas ρ_2 and C_2 are for water.

For the BI simulations, the typical distance of a bubble's center to the wall is estimated from high-speed side-view recordings as reported by Fernandez Rivas *et al.*[28] and is taken to be $25 \mu m$. The absolute driving pressure obtained in our previous study[28] was 130 kPa, superimposed on the ambient pressure of 1 bar. These values are used in the BI code, which results in a collapse as shown in Figure 3. The final moments simulated in the BI code, for a single bubble of radius $2 \mu m$, predicted a collapse time from maximum radius to zero of approximately $0.1 \mu s$ (Figure 3). The final velocity of the bubble wall at the point where the BI code stopped was of the order of $10^2 m/s$. The associated water hammer pressure was calculated to be of the order of 0.1–1 GPa; the shear stress was of the order of 0.1–1 MPa.
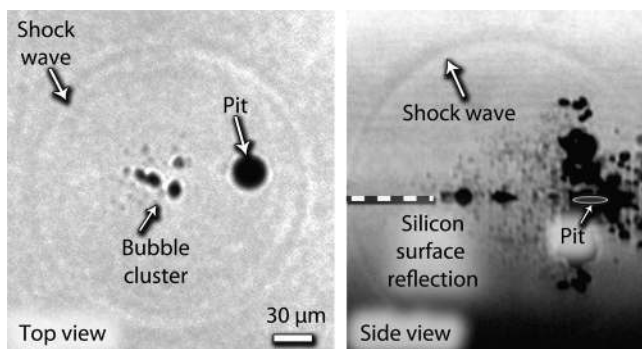

FIG. 4. Top and side view of bubbles cavitation close to the silicon surface with the emission of a shock wave originated from the bubble clusters. The exposure time for the illumination of this experiment was 7 ns, more details of this method can be found elsewhere.[28] A dashed line indicates the position of the silicon surface.

As a general trend, smaller bubbles (in the simulated range of 2–$25 \mu m$ in radius) resulted in higher collapse velocities, due to the larger curvature. A larger initial distance γ of the bubble from the wall also resulted in higher collapse velocities, with the limit at large γ approaching the non-wall-bound spherical bubble collapse velocity.

The collapse evolution calculated by the BI code for a single bubble of radius $15 \mu m$ near a wall was compared to that of a similar bubble of similar size in the ultra high-speed recording. The collapse time of the bubbles in experiment was of the order of $1 \mu s$, which is a similar collapse time as predicted by the BI code. More details can be found in the Appendix.

The presence of shock wave emissions can be seen in the short exposure photos, see Figure 4. This observation was feasible since the refractive index gradient induced by the shock front in the liquid refracts the illumination light. The shock wave width could not be measured properly with the available conditions, nor its propagation speed (details on this experimental setup can be found elsewhere).[28] The width of the shock wave image should not be mistaken for the shock wave width.[34]

Erosion observations of different crystallographic surfaces of silicon

A perspective inclined view for the case of (100) Si can be seen in Figure 5 after cavitation exposure for 180 min. Each SEM image showed features depending on the crystallographic orientation; how they form and evolve in time is related to the crystal lattice properties (see Table I). For all orientations, we can describe two distinctive types of erosion effects. One is "erosion pitting" and the second is "fracture lines."

If one compares Figure 1 and advanced erosion stages as in Figure 6, it is possible to observe that for (100) Si, the superficial fracture lines are perpendicular, for (110) the lines have an angle of approximately 54.3° in between and for (111) an angle of 60°.

Orientation (100)

A three-dimensional schematic view is provided in Figure 7 and compared with SEM images after various times of ultrasound exposure of (100) Si. The red lines represent needle-like cracks which result in grain detachment starting after 50 min. The grains of material detached resemble in most cases a pyramidal shape, as can be seen in detail after 180 min (formed by the {111} planes).

It was not possible to obtain a cross-sectional analysis of the surfaces. Nevertheless, close to the verge of the pit's edge and SEM tilted images (see Fig. 5), it is possible to gain some understanding of how the crack lines connect underneath the flat top (100) surface, as depicted in Figure 8. From these detailed figures we can understand that the erosion process is not restricted to superficial damage, but also can have effects in the bulk.

All the {111} are inclined with respect to the (100) surface (top surface of the Si substrate). The surface energy and fracture toughness of {111} planes are the lowest, making it energy-wise more probable to create a new surface than in
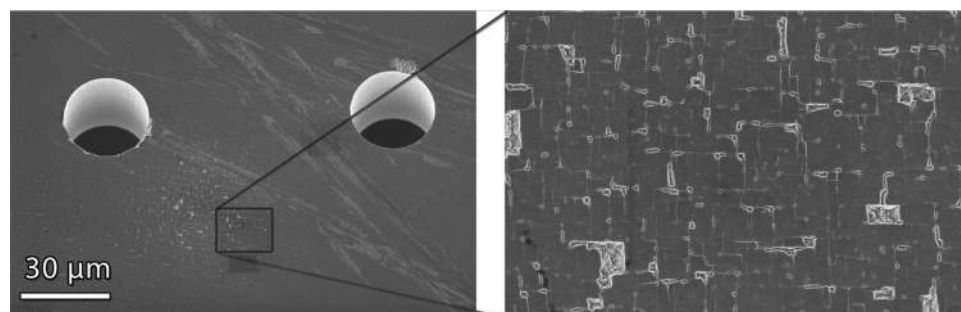
FIG. 5. An inclined view of a SEM image showing the eroded area in the vicinity of the two pits in a (100) substrate. A zoomed in view to the right side shows the typical erosion features after 180 min.

other crystallographic planes (see Table I). The intersecting lines make a 90° angle.

A certain regularity was observed but not quantified in the distance between the cleavage lines, which got smaller with time. It is recommended for future studies to quantify the location and spread of these lines over time across the whole surface.
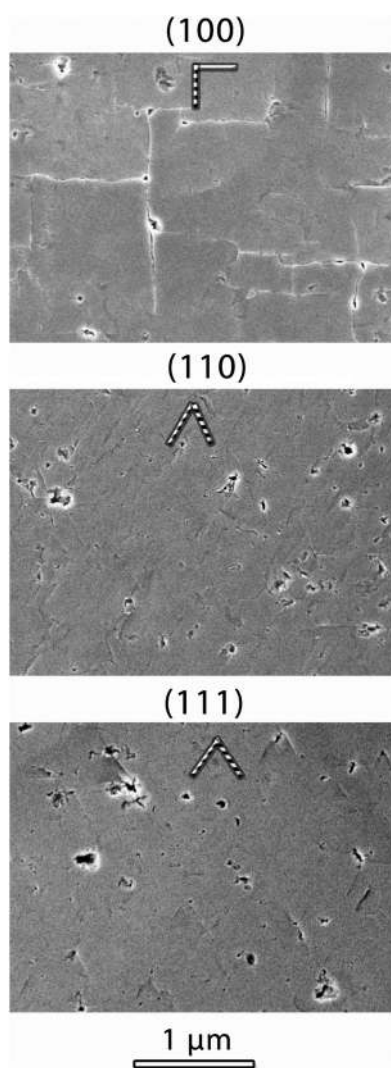

FIG. 6. Comparison of the observed advanced erosion fracture lines for (100), (110), and (111) silicon after 180 min of cavitation exposure. The drawn bars indicate the directions followed by the majority of cracks and correspond approximately to Figure 1. For (100) these lines are perpendicular, for (110) a combination of ⟨110⟩ and ⟨1$\bar{1}$2⟩ directions complying with (111) cleavage planes at 54.3° is observed, and for (111) the lines have an angle of 60° and directions ⟨110⟩.

Orientation (110)

Erosion pits and crack lines show different features on (110) compared to (100) Si at the early stages. Some details can be observed in Figure 9.

There are two types of {111} intersecting the (110) surface of the substrate: Those that intersect the (110) along [$\bar{1}$10] are inclined with respect to (110) and those that intersect the (110) along [1$\bar{1}$2] or [$\bar{1}$12] that are oriented perpendicular to (110).

Based on our observations, the most probable places to develop cracks are at the intersections of [$\bar{1}$10] and one of the other two intersection locations. The intersecting lines make an angle of 54.3°, 71.4°, and 125.7° on the (110) surface.

The most striking observation is perhaps the zig-zag crack shown in Figure 9(b). Such behavior can be understood from literature, as Vicker's indentation tests for the {110} indent plane show that the crack "intended" to propagate on the {1$\bar{1}$0} planes zig-zags mainly on the {1$\bar{1}$1} planes.[44,52]

Orientation (111)

In the case of (111), the erosion pits and crack lines show a clear difference compared to the two other crystal orientations at the early stages shown in Figure 10. The most salient is that crack lines (sometimes six) can intersect and merge in a given point.

There are three {111} types of planes intersecting the (111) and as will be shown later, these are all likely to grow cracks. The intersecting lines make an angle of 60° on the (111) surface in agreement with the situation depicted in Figure 10.

Erosion by an ultrasonic horn

Exposure to the ultrasonic horn also resulted in erosion of the silicon surfaces (100) and (110) (Fig. 11), but the eroded parts were not as concentrated as in the micro-pit experiments. The erosion pits look larger for the same sonication period. Evidently, the effect of a lower frequency has a strong influence on the mechanical damage when compared to higher frequencies as employed for the micropits setup. For (111), there was no damage that could be imaged at least after 10 min. Longer exposure time experiments were not conducted as it was reported that for 20 kHz and a horn cavitation system the incubation period is larger (4 h).[18] This can be attributed to the differences in the dynamic loading and physico-chemical conditions given by our setup compared to the horn.
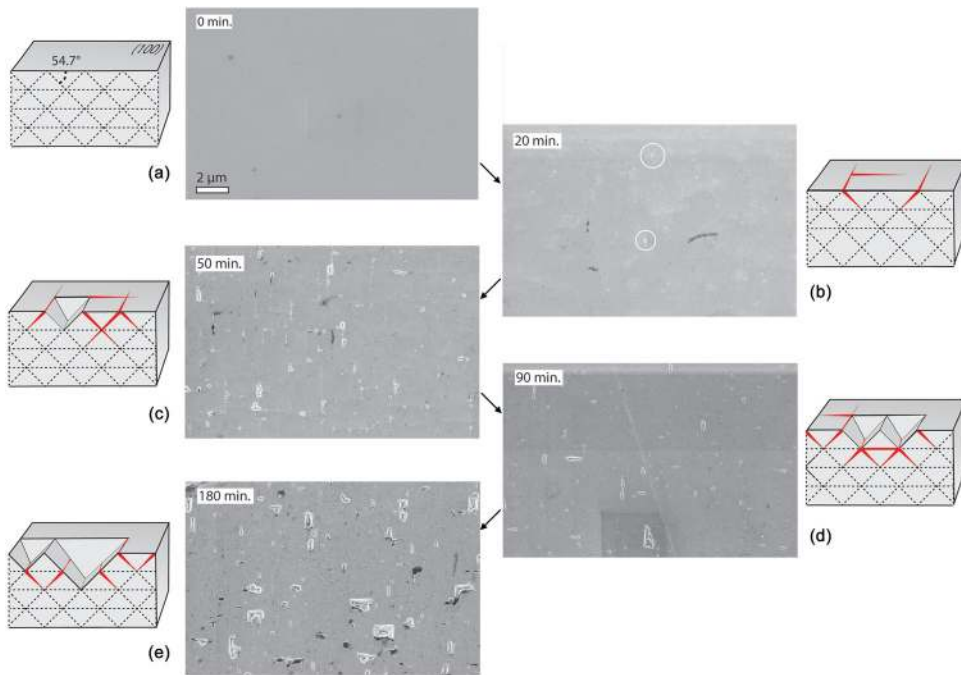
FIG. 7. Comparison of an artistic description of the erosion characteristics with the erosion progression in (100) Si wafer, at five different erosion times (a-e). The shape of the erosion pits at 180 min shows a pyramidal shape in agreement with the orientations of {111} planes. The white circles at 20 min mark the small cracks observed at early stages.

DISCUSSION

Study of Si fatigue

Even though erosion and fatigue studies in silicon are available in the literature, a one-to-one comparison with our results cannot be given (different types of loading, frequency, test duration). For that reason, we consider it important to try to provide some reference values and discussions on this subject.

Each collapsing bubble that was produced by the micro-pit ultrasound device results in a force load on the silicon surface (either a liquid jet or shockwave). Each load by itself may not be enough to fracture the silicon, but repeated loading can lead to fatigue failure. Figure 3 of Varvani-Farahani's work[52] shows an S/N curve (stress vs. number of loads), without an empirical fitting factor.[52,57,73] Using this curve, we can estimate the number of bubbles (loads, N) needed to make the material fail. The BI method for single bubble collapse near a wall predicted a water hammer pressure ranging from 0.1 to 1 GPa, which corresponds to a number of loads (N) larger than 10^8. Using the estimated number of bubble impacts as described in Sec. III A, along 50 min, when clear damage to the surface is observed, leads to a number of impacts in the order of 10^6. If we consider all these impacts to be loads on a single point, Si would fail if each impact would be of ∼2.4 GPa.

From these values, we can only say that the order of magnitudes of the water hammer jets the BI code provides is relatively close to the expected stresses known to make Si fail by virtue of fatigue effects. However, the contribution of shock waves cannot be ruled out.

The pressure exerted on an AFM tip by bubble clusters similar to the ones given here was estimated to be ∼5 MPa.[10] This should be taken as a lower estimate since the distance from the silicon substrate from which the bubbles were generated to the AFM tip was ca. 100 μm, instead of collapsing near the silicon surface as this study has covered.

When comparing the stresses provided by shock waves reported in literature (10 GPa (Ref. 34)), with the *S/N* curves of Varvani's methodology[52] it is not possible to get a value of loads *N*, because the lowest amount of cycles accounted was ∼200, corresponding to roughly 2.8 GPa stress value. If the shock waves impacting the Si surfaces in this study would exert a 10 GPa stress value, that would certainly make Si fail from the first impact; but in reality the zone of impact is embedded in a larger material matrix, making it a more complex situation than a free-standing piece used in other fatigue experiments. We can speculate that the type of bubble collapse encountered in our experiments is different than for the conditions at which those high pressure values were measured; the most important being that we have a bubble cluster collapse, and in those cases, bubbles experience a "shielding effect" that may lead to reduced shock wave pressures.[42,74] Interestingly, the metallization of c-Si with shock-waves has been described.[75]
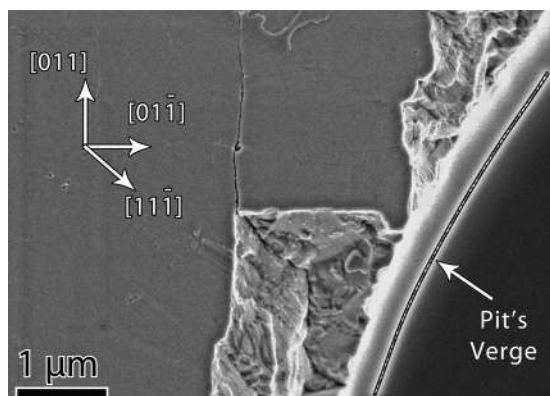

FIG. 8. Deep cracks at the verge of the pit along {111} planes in (100) silicon near a micromachined pit, after 50 min irradiation.
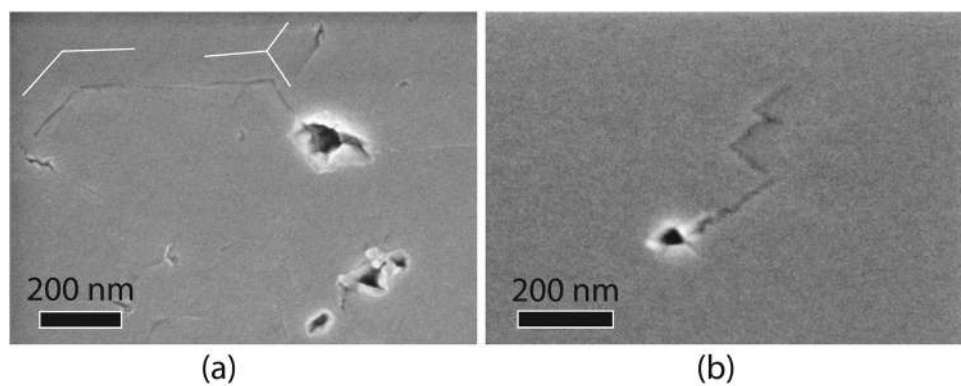
FIG. 9. Details of erosion in (110) Si wafer in the early stages (less than 100 min). Observe the presence of erosion pits and some cracks having particular shapes: (a) lines close to the erosion pits of a length of 200 nm and (b) zig zag cracks with orientations in the [1$\bar{1}$2], [$\bar{1}$12], and [$\bar{1}$10] directions.
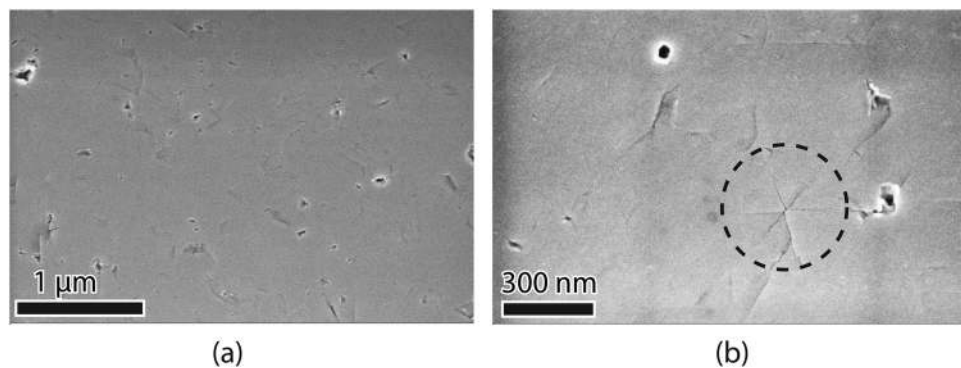

FIG. 10. Details of erosion in (111) Si wafer at early stages of erosion (less than 100 min). (a) Small crack lines connect in small cornered grooves and small erosion pits scattered on the surface. (b) Six crack lines intersect and merge in a given point highlighted by a dashed circle.

From the results of Virot and coworkers[18] on Si cavitation erosion, a better resistance to cavitation erosion of Si was found when compared to glass, having long incubation times (~4 h). In general, even though pits and cracks were formed, the final erosion state differed from other materials, like glasses or metals. The superhydrophilicity of the surface after sonication was explained as a result of increased density of hydroxyl groups at the newly created surfaces or perhaps an inverse lotus effect. Shifts in the Raman spectra

FIG. 11. Details of the erosion in (100) Si wafer (a) and (110) (b) at early stages of erosion (10 min exposure at 20 kHz).

pointed at anisotropic compressive stresses along with lattice deformation; deconvolution analysis gave evidence of the presence of grain boundaries or crystalline Si particles, the coexistence of crystalline Si (c-Si), and amorphous Si (a-Si). The latter was correlated to plastically deformed areas observed with SEM, and may result from a loss of lattice stability during the cyclic compressions/decompressions exerted by the collapse of bubbles. TEM analysis coincided with SEM results, and additionally revealed a more complex highly stressed and distorted structure, showing several possible phases: c-Si, a-Si, and polycrystalline Si (poly-Si). It was also concluded that local changes in Si, like amorphization and metalization, could fracture, deform, and dislocate the Si sub-surface. This could in turn change its density leading to volume expansion and contraction affecting the electron density of states (thermal and electrical properties of Si) promoting the emission of Ar^* by mechanoluminescence. Contrary to other studies found in literature, no aging effect of Si in pure water for several days or in parts not directly exposed to US was found.

To complete this study, further experiments might be conducted in the future to measure the effect of shock waves and surface erosion evolution. All these phenomena are certainly interconnected and may have a synergistic effect towards erosion of Si surfaces.

The ultimate cause for fatigue of Si, as a brittle material, would be the damage accumulation (formation and propagation of cracks) as a result of small stress loads (either jet or shockwave impact), aggravated by the chemical corrosion effects of the products of sonochemical products of bubble cavitation. Wave propagations as a result of the pressure pulses against the Si surface may contribute to the complex erosion scenario.
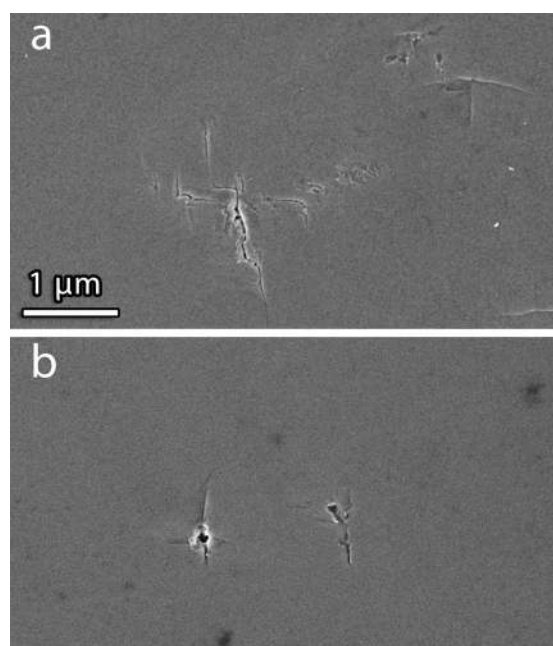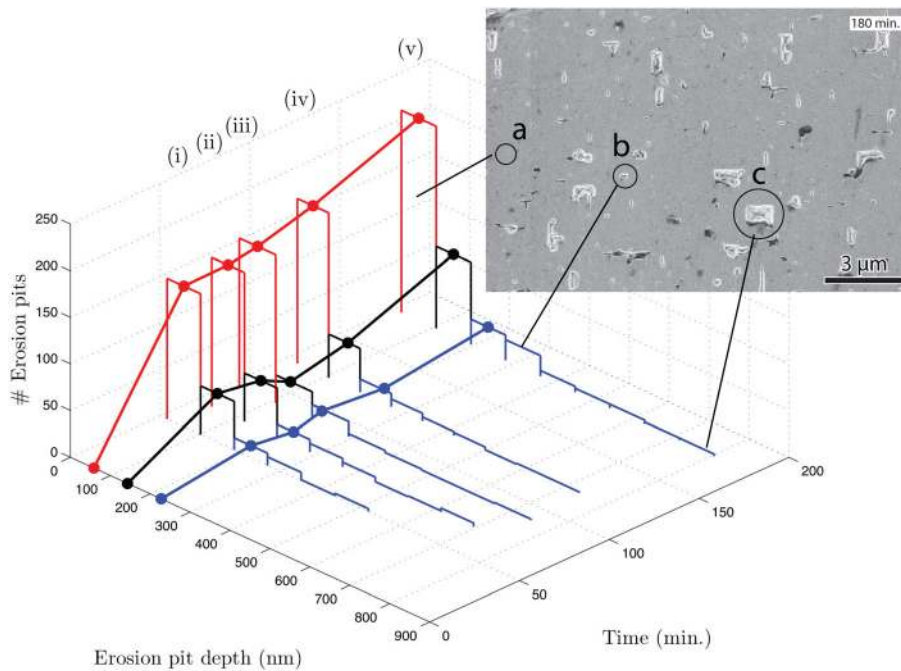
FIG. 12. Histogram plots of the calculated erosion pit depth in (100) silicon as a function of the number of erosion pits and the irradiation time: (i) 50 min, (ii) 70 min, (iii) 90 min, (iv) 120 min, and (v) 180 min. The first three histogram bins are colored and connected to show their particular evolution. The image resolution did not allow pit depth extraction for irradiation times below 50 min.

Area and volume erosion

The eroded volumes calculated from SEM images are shown in Figure 12. The growth and interconnection (coarsening) of small erosion pits create deep crater-like erosion pits. The amount of smaller erosion pits increases with time (type a) and other larger erosion pits are formed by coalescence (b and c). For instance, the amount of erosion pits with depths 100–200 nm (black line) shows a decline after 50 min and at the same time, deeper erosion pits (>500 nm) increase in number. This can be understood as a cascading effect that indicates what seems to be the end of the incubation period.

The erosion features for (110) and (111) were completely different. Smaller in number and eroded area and no clear geometrical figure could be related to the shape of the pits. Hence, a similar assessment of erosion pit depth as for (100) was not possible.

Comparing the number of erosion pits and eroded area calculated in Sec. II E, (100) clearly shows a qualitatively different progression in the erosion process compared with (110) and (111). In all three cases, the initial stage seems to be consistent with the presence of small cracks (small openings on the surface) that upon the action of the collapse of cavitation bubbles, start to grow. As the cavitation exposure progresses, these cracks grow and interconnect; (100) show a more pronounced presence of superficial cracks. These cracks can reach deep into the crystal bulk (as seen in Fig. 8) and eventually, while the erosion pits also grow in area or volume, the "weaker" planes start to intersect (in a pyramidal fashion matching the {111} planes) making it possible for a grain or piece of material to detach. The large detached material (which presumably could have contained at least four erosion pits) forms a new and larger pit, reducing the total number N of erosion pits (see Fig. 13).

For (110) and (111), the situation seems different. We see that the way the cracks and planes intersect, indeed allows for the formation of erosion pits, but not in a pyramidal shape as cavitation exposure increases (which is the case for (100)). Interestingly, the existing pits do not interconnect in the same fashion, giving an increase in the number of pits, but not an increase in the area (crack propagation is impeded), as is the case for (100) (see Fig. 14).

Plotting the relative eroded area divided by the number of erosion pits, which we define as $\alpha_p = \frac{\Delta A}{A}/N$, gives insight into the coarsening progression, i.e., interconnection of the erosion pits. Fig. 15 clearly shows the differences among (100) compared with (110) and (111), where these last two show a similar and relatively horizontal slope, whereas after the incubation time (50 min), (100) increases with a higher slope. Note that we define the incubation time as the time in which all the analyzed parameters show clear differences for each silicon crystallographic configuration. Other authors
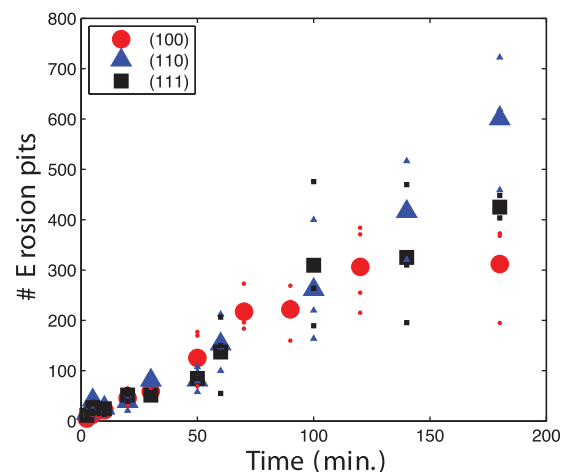

FIG. 13. Absolute number of erosion pits as a function of the sonication exposure time. The scattered points are individual substrate measurements and the bold symbol represents the averaged value for that specific sonication time.
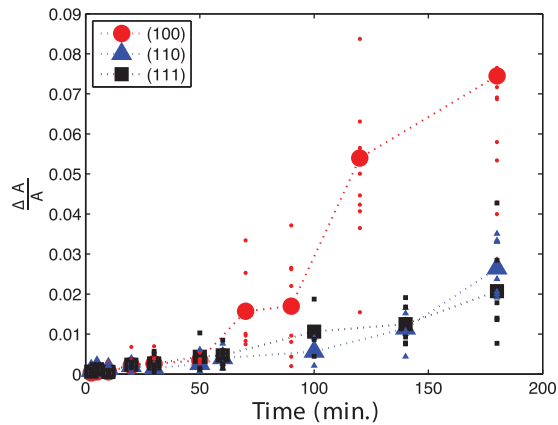
FIG. 14. Relative eroded area ($\frac{\Delta A}{A}$) plotted as a function of sonication exposure time. The scattered points are individual measurements and the bold symbol represents the averaged value for that specific sonication time.

use line extrapolation from their erosion rate plots in the acceleration stage,[50] but we are not using this approach because the time span and trends we observe are not conclusive to know which period of erosion has been reached. Other papers reported a longer resistance to erosion,[18] which from our horn cavitation preliminary measurements appears to be the case for lower frequencies and a similar cavitation system as shown in Fig. 11.

When considering the physical properties of the materials studied here (see Table I), we can see that the modulus of elasticity for {100} is 1.5× and 1.8× smaller than {110} and {111}, respectively. The ability of absorbing forcing loads (either liquid jets or shockwaves) seems to be related to the fact that (100) erodes faster. In literature it is reported that Vicker's indentation performed on (100) surfaces, shows higher hardness (resistance to permanent deformation) and lower toughness (ability to absorb energy and deform in a plastic fashion without fracturing) for (100).[44] This can explain why (100) shows more fragile behavior. But it must also be noted that the dynamic type of loading of cavitation is faster than indentation tests, which can certainly have an influence on the type of erosion.[18]
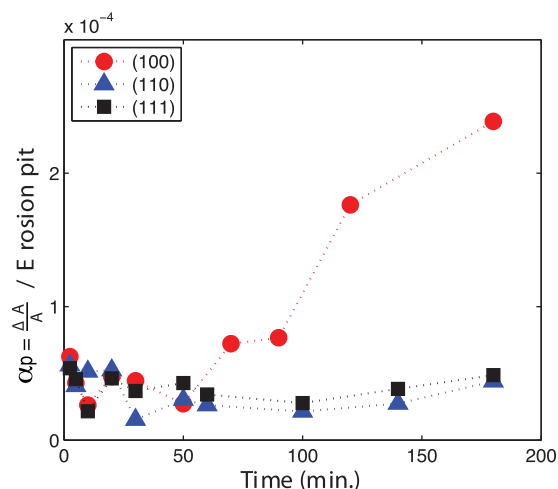

FIG. 15. Plot of α_p (relative eroded area divided by the number of erosion pits) as a function of sonication exposure time.

According to literature, the fracture toughness is approximately the same for the three crystal orientations. This might be connected to the fact that the presence of pre-existing cracks, and the appearance of new cracks, follows a similar trend in all cases (Fig. 13).

The marked difference of (100) having extended crack lines and detachment of small grains not observed in the other silicon substrates with different crystallographic orientation needs further discussion. Based on our observations it is assumed that damage formation on {111} is related to shear forces acting on these planes as a result of jetting, shockwaves or any other loading of the Si surface. If the damaging force acts perpendicular to the Si single crystal surface, the resulting maximum shear stress on {111} is proportional to $\sin 2\phi$. This expression can be derived from the Schmid factor m that relates the applied stress σ to the resolved shear stress τ on a slip plane for a dislocation moving in a certain slip direction: $\tau = m\sigma$. It is defined as $m = \cos(\phi)\cos(\lambda)$, with ϕ the angle between the applied load and the slip plane normal and λ the angle between the applied load and the slip direction. Since the exact cause of damage formation on {111} is not completely clear and might not be directly related to dislocation movement, an indicative value of the Schmid factor can be obtained assuming damage to occur in the direction of maximum shear stress. This direction is obtained by decomposing the applied force unit vector in a component perpendicular to and parallel with the {111} plane. The first component is in the direction of the slip plane normal and defines the normal stress on {111}. It is proportional to $\cos \phi$ which is also equal to the first term of the Schmid factor. The second component is parallel to the slip plane and defines the shear stress on {111}. It is proportional to $\sin \phi$ and constitutes the second term of the Schmid factor. The product of both terms leads to the $\sin 2\phi$ dependence.

It can be concluded that damage formation on {111} planes for Si (100) is most probable, since the corresponding value of $\sin 2\phi$ is largest. Experimental evidence, such as shown in Fig. 14, supports this idea. Furthermore, Fig. 15 shows that after some incubation/nucleation time rapid growth of the eroded area of an erosion pit occurs. The collective damage formation on all {111} planes at a (100) surface results in pyramidal shaped grains that can break off consecutively. In this way, cracks can grow out easily from an erosion pit to form fracture lines. For Si (110) such a mechanism is less likely, as under the action of the damaging force perpendicular to the (110) surface, only two {111} are active, i.e., $\sin 2\phi > 0$. For grains to break off more than two active {111} are required, four for (100) as can be seen in Fig. 7. For Si (111) three {111} are active, but the value of $\sin 2\phi$ and the number of active {111} are smaller than for Si (100), making damage growth slower. It would be interesting to extend the sonication exposure time to see the development of α_p in time for Si (110) and Si (111).

Following the same methodologies as reported by Virot *et al.*[18] using TEM, micro-Raman, and X-ray diffraction would provide more useful information on the changes due to sonication occurring in all crystallographic Si substrates.

Ultrasound erosion systems

To illustrate the advantages of using the device with micromachined pits over conventional testing apparatuses, we compared it with the horn experiments we conducted. First, the amount of water used is 10^3 larger which, depending on the number of experimental tests, and the purity of water or other liquid used, can result in significant costs. Second, as the area exposed to the horn cavitation conditions is considerably larger, the erosion features were more difficult to locate and image with SEM. The lower frequency apparently influenced the erosion of (111) substrates for which no damage could be found for the studied times. Furthermore, the conditions to hold the horn and the substrates in place were more difficult to control, hence in a more complex experimental measurement strategy, reproducibility would be affected. Additionally, it is not straightforward to image the events of bubble cavitation in the small gap between the horn and the exposed substrate. For complimentary information on a horn system used to study the (100) erosion and other phenomena like mechanoluminescence and phase changes on silicon structure (amorphization), we refer the reader to the literature.[18]

CONCLUSIONS

With the setup described in this work, we demonstrate its advantages to study cavitation in well controlled conditions. A detailed study can be performed on the erosion at the microscale during the incubation period. Even though we used a reduced set of conditions to carry this study, focusing more on the material's erosion side, several parameters such as frequency, pressure amplitude, gas content, and liquid type can be varied to address the cavitation erosion effects of bubbles on several types of materials, besides silicon. It also offers advantages over conventional experimental setups like sonicators (baths or horns), hydrodynamic flows or jets cavitation erosion test, in the sense that the current setup uses smaller volumes, allows the direct recording of the phenomena involved, and the location of cavitation bubbles can be better controlled. The possibility to study cavitation erosion, right from the initial incubation period and through more advanced stages (180 min) has been demonstrated in Si with the help of micromachined pits.

We observed that the concerted effect of various sources of damage formation such as jetting, shock waves, direct bubble impact, and surface stress corrosion can all cause the damage observed for the three crystallographic silicon surfaces studied, although each of the three surfaces have a different resistance to erosion. For (100) silicon, and under the current working conditions, the incubation time was of the order of 50 min, whereas for (110) and (111) apparently the incubation period is larger than the total 180 min sonication. A possible explanation for this occurrence has been provided.

The design of an experiment in which each of the cavitation damage mechanisms can be isolated will be a challenge for future research. These studies could be carried out at different powers and other materials with an improved imaging system to better quantify the shock wave emissions.

APPENDIX: BOUNDARY-INTEGRAL CODE FOR SIMULATION OF A BUBBLE COLLAPSING NEAR A WALL

The collapse of a spherical bubble can be simulated using an axisymmetric boundary integral (BI) method, which has been shown to be able to predict the collapse of single and multiple bubbles.[76] The numerical simulations assume potential (irrotational, incompressible, inviscid) flow around the bubble till the straight solid (impermeable) wall with length much larger than the initial bubble radius R. The axisymmetric bubble contour is described using cylindrical coordinates r, z and is solved numerically. The simulations are based on the numerical code described elsewhere.[77–80] The dynamic boundary condition on the droplet contours is the unsteady Bernoulli equation

$$\left(\frac{\partial \phi}{\partial t} + \frac{1}{2}|\nabla \phi|^2\right) = -gz - \frac{\gamma}{\rho_l}\kappa(r,t) - \frac{P_{ext} - P_\infty}{\rho_l}. \quad \text{(A1)}$$

Here, ϕ is the flow potential ($\nabla \phi = \vec{u}$, $\vec{u}$ being the local velocity vector), t is time, g the acceleration of gravity, z the absolute height, γ the surface tension, ρ_l the density of the liquid, $\kappa(r,t)$ the interface curvature, $P_{ext}(r,t)$ the external liquid pressure applied on the bubble, and P_∞ the far field pressure. The initial conditions for the simulations consist of a spherical bubble with radius R, distance d from the solid wall, under influence of a pressure P_{ext}.

The BI code was checked by obtaining the evolution of the maximum bubble radius of a symmetric collapsing bubble (no wall, or $d \gg R$) during the simulation. This
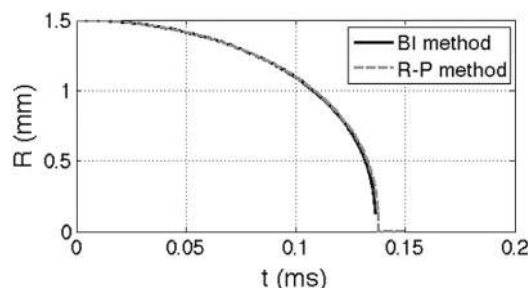

FIG. 16. R(t) curve for a 1.5 μm initial radius spherical bubble far away from any wall, as simulated with the BI code (black solid line) and a Rayleigh-Plesset model (gray dashed line).

radius-time curve was compared against the radius-time curve for a single, spherical bubble as predicted by the Rayleigh-Plesset equation,[81] simulated in MATLAB using the ODE45 function. The result is plotted in Figure 16 and shows good agreement between the two methods.

Another validation was performed by simulating the collapse of a millimeter-sized laser-induced bubble near a solid wall, as studied by Brujan *et al.*,[40] who reported a jet velocity of 130 m/s for a bubble of radius 1.5 mm and a distance of 2.5 mm from the wall. The BI simulation resulted in a final velocity of order 10^2 m/s.

[1] K. Suslick, *Encyclopaedia Britannica Yearbook of Science and the Future* (Encyclopaedia Britannica, Chicago, 1994), pp. 138–155.

[2] D. Lohse, Phys. Today **56**, 36 (2003).

[3] L. Rayleigh, Philos. Mag. Ser. 6 **34**, 94 (1917).

[4] C. Brennen, *Cavitation and Bubble Dynamics*, Oxford Engineering Science Series (Oxford University Press, 1995).

[5] F. Lugli and F. Zerbetto, Phys. Chem. Chem. Phys. **9**, 2447 (2007).

[6] T. Graf, H. Fischer, H. Reul, and G. Rau, Int. J. Artif. Organs **14**, 169 (1991).

[7] R. Arndt, Annu. Rev. Fluid Mech. **13**, 273 (1981).

[8] D. Dowson and C. M. Taylor, Annu. Rev. Fluid Mech. **11**, 35 (1979).

[9] M. O. Lamminen, H. W. Walker, and L. K. Weavers, J. Membr. Sci. **237**, 213 (2004).

[10] D. F. Rivas, B. Verhaagen, J. R. T. Seddon, A. G. Zijlstra, L.-M. Jiang, L. W. M. van der Sluis, M. Versluis, D. Lohse, and H. J. G. E. Gardeniers, Biomicrofluidics **6**, 034114 (2012).

[11] M. Virot, T. Chave, S. I. Nikitenko, D. G. Shchukin, T. Zemb, and H. Möhwald, J. Phys. Chem. C **114**, 13083 (2010).

[12] C. Haosheng, L. Yongjian, C. Darong, and W. Jiadao, Tribol. Lett. **26**, 153–159 (2007).

[13] T. J. Mason, A. J. Cobley, J. E. Graves, and D. Morgan, Ultrason. Sonochem. **18**, 226 (2011).

[14] A. El-Bahar, S. Stolyarova, A. Chack, R. Weil, R. Beserman, and Y. Nemirovsky, Phys. Status Solidi A **197**, 340 (2003).

[15] E. V. Skorb, D. G. Shchukin, H. Möhwald, and D. V. Andreeva, Nanoscale **2**, 722 (2010).

[16] G. G. A. Fatjo, M. Hadfield, and K. Tabeshfar, Ceram. Int. **37**, 1919 (2011).

[17] A. Podolian, A. Nadtochiy, V. Kuryliuk, O. Korotchenkov, J. Schmid, M. Drapalik, and V. Schlosser, Sol. Energy Mater. Sol. Cells **95**, 765 (2011).

[18] M. Virot, R. Pflieger, E. V. Skorb, J. Ravaux, T. Zemb, and H. Möhwald, J. Phys. Chem. C **116**, 15493 (2012).

[19] J. Koshka, S. Ostapenko, T. Ruf, and J. M. Zhang, Appl. Phys. Lett. **69**, 2537 (1996).

[20] S. Kalem, O. Yavuzcetin, and C. Altineller, J. Porous Mater. **7**, 381 (2000).

[21] E. V. Skorb, D. V. Andreeva, and H. Möhwald, Angew. Chem., Int. Ed. **51**, 5138 (2012).

[22] J. Rooze, E. V. Rebrov, J. C. Schouten, and J. T. Keurentjes, Ultrason. Sonochem. **18**, 209 (2011).

[23] E. Zwaan, S. Le Gac, K. Tsuji, and C.-D. Ohl, Phys. Rev. Lett. **98**, 254501 (2007).

[24] D. F. Rivas and J. G. E. Gardeniers, ASME Conf. Proc. 2008, 1939.

[25] S. Howkins, J. Acoust. Soc. Am. **39**, 55 (1966).

[26] N. Bremond, M. Arora, C. D. Ohl, and D. Lohse, Phys. Rev. Lett. **96**, 224501 (2006).

[27] D. Fernandez Rivas, A. Prosperetti, A. G. Zijlstra, D. Lohse, and H. J. G. E. Gardeniers, Angew. Chem., Int. Ed. **49**, 9699 (2010).

[28] D. Fernandez Rivas, L. Stricker, A. G. Zijlstra, H. J. G. E. Gardeniers, D. Lohse, and A. Prosperetti, Ultrason. Sonochem. **20**, 510 (2013).

[29] T. B. Benjamin and A. T. Ellis, Philos. Trans. R. Soc. London, Ser. A **260**, 221 (1966).

[30] A. Philipp and W. Lauterborn, J. Fluid Mech. **361**, 75 (1998).

[31] M. Dular and A. Osterman, Wear **265**, 811 (2008).

[32] C. M. Preece and J. H. Brunton, Wear **60**, 269 (1980).

[33] E. A. Brujan, G. S. Keen, A. Vogel, and J. R. Blake, Phys. Fluids **14**, 85 (2002).

[34] E. A. Brujan, T. Ikeda, and Y. Matsumoto, Exp. Therm. Fluid Sci. **32**, 1188 (2008).

[35] A. Brotchie, F. Grieser, and M. Ashokkumar, Phys. Rev. Lett. **102**, 84302 (2009).

[36] M. Ashokkumar, J. Lee, Y. Iida, K. Yasui, T. Kozuka, T. Tuziuti, and A. Towata, ChemPhysChem **11**, 1680 (2010).

[37] C. J. B. Vian, P. R. Birkin, and T. C. Leighton, J. Phys. Chem. C **114**, 16416 (2010).

[38] S. N. Buravova and Y. A. Gordopolov, Int. J. Fract. **170**, 83 (2011).

[39] N. K. Bourne, Shock Waves **11**, 447 (2002).

[40] E.-A. Brujan, K. Nahen, P. Schmidt, and A. Vogel, J. Fluid Mech. **433**, 283 (2001).

[41] C.-D. Ohl, A. Philipp, and W. Lauterborn, Ann. Phys. **507**, 26 (1995).

[42] D. Fernandez Rivas, M. Ashokkumar, T. Leong, K. Yasui, T. Tuziuti, S. Kentish, D. Lohse, and H. J. Gardeniers, Ultrason. Sonochem. **19**, 1252 (2012).

[43] N. C. Eddingsaas and K. S. Suslick, Nature **444**, 163 (2006).

[44] F. Ebrahimi and L. Kalwani, Mater. Sci. Eng., A **268**, 116 (1999).

[45] N. Maluf, *An Introduction to Microelectromechanical Systems Engineering* (Artech House, 2000).

[46] G. G. A. Fatjo, M. Hadfield, C. Vieillard, and J. Sekulic, Ceram. Int. **35**, 3301 (2009).

[47] B. Karunamurthy, M. Hadfield, C. Vieillard, and G. Morales, Tribol. Int. **43**, 2251 (2010).

[48] C. G. Stephanis, J. G. Hatiris, and D. E. Mourmouras, Ultrason. Sonochem. **4**, 269 (1997).

[49] J.-P. Franc and J.-M. Michel, *Fundamentals of Cavitation*, Fluid Mechanics and Its Applications (Kluwer, 2004).

[50] S. Hattori, T. Hirose, and K. Sugiyama, Wear **269**, 507 (2010).

[51] C. L. Muhlstein, S. B. Brown, and R. O. Ritchie, J. Microelectromech. Syst. **10**, 593 (2001).

[52] A. Varvani-Farahani, Microsyst. Technol. **11**, 129 (2005).

[53] K. Komai, K. Minoshima, and S. Inoue, Microsyst. Technol. **5**, 30 (1998).

[54] S. M. Wiederhorn, S. W. Freiman, E. R. Fuller, and C. J. Simmons, J. Mater. Sci. **17**, 3460 (1982).

[55] T. Okada, Y. Iwai, S. Hattori, and N. Tanimura, Wear **184**, 231 (1995).

[56] J. Steller, Wear **233**, 51 (1999).

[57] A. Varvani-Farahani, Int. J. Fatigue **22**, 295 (2000).

[58] C. Chin, C. Lancée, J. Borsboom, F. Mastik, M. Frijlink, N. de Jong, M. Versluis, and D. Lohse, Rev. Sci. Instrum. **74**, 5026 (2003).

[59] A. van der Bos, A. Zijlstra, E. Gelderblom, and M. Versluis, Exp. Fluids **51**, 1283 (2011).

[60] J. H. Brunton, Philos. Trans. R. Soc. London, Ser. A **260**, 79 (1966).

[61] S. S. Cook, Proc. R. Soc. London, Ser. A **119**, 481 (1928).

[62] C.-D. Ohl, M. Arora, R. Ikink, N. De Jong, M. Versluis, M. Delius, and D. Lohse, Biophys. J. **91**, 4285 (2006).

[63] E. A. Brujan, T. Ikeda, K. Yoshinaka, and Y. Matsumoto, Ultrason. Sonochem. **18**, 59 (2011).

[64] M. Brede and P. Haasen, Acta Metall. **36**, 2003 (1988).

[65] G. Michot and A. George, in *Structure and Properties of Dislocations*, edited by S. G. Roberts, D. B. Holt, and P. R. Wilshaw (IOP, 1989), Vol. 104, pp. 385–396.

[66] A. George and G. Michot, Mater. Sci. Eng., A **164**, 118 (1993).

[67] P. B. Hirsch, S. G. Roberts, and J. Samuels, Proc. R. Soc. London, Ser. A **421**, 25 (1989).

[68] C. S. John, Philos. Mag. **32**, 1193 (1975).

[69] M. Tanaka, K. Higashida, H. Nakashima, H. Takagi, and M. Fujiwara, Int. J. Fract. **139**, 383 (2006).

[70] P. J. Hesketh, C. Ju, S. Gowda, E. Zanoria, and S. Danyluk, J. Electrochem. Soc. **140**, 1080 (1993).

[71] C. Thaulow, S. V. Schieffer, I. R. Vatne, D. Sen, and E. Ostby, Comput. Mater. Sci. **50**, 2621 (2011).

[72] C. Chen and M. H. Leipold, Am. Ceram. Soc. Bull. **59**, 469 (1980).

[73] Y. Wang and W. Yao, Int. J. Fatigue **26**, 17 (2004).

[74] S. Hatanaka, K. Yasui, T. Kozuka, T. Tuziuti, and H. Mitome, Ultrasonics **40**, 655 (2002).

[75] S. D. Gilev and A. M. Trubachev, J. Phys.: Condens. Matter **16**, 8139 (2004).

[76] N. Bremond, M. Arora, S. M. Dammer, and D. Lohse, Phys. Fluids **18**, 121505 (2006).

[77] H. N. Oguz and A. Prosperetti, J. Fluid Mech. **257**, 111 (1993).

[78] R. P. H. M. Bergmann, D. van der Meer, S. Gekle, J. van der Bos, and D. Lohse, J. Fluid Mech. **633**, 381 (2009).

[79] S. Gekle and J. Gordillo, Int. J. Numer. Methods Fluids **67**, 1456 (2011).

[80] W. Bouwhuis, R. van der Veen, T. Tran, D. Keij, K. Winkels, I. Peters, R. van der Meer, C. Sun, J. Snoeijer, and D. Lohse, Phys. Rev. Lett. **109**, 264501 (2012).

[81] T. Leighton, *The Acoustic Bubble* (Academic, London, 1994).